Research in Astronomy and Astrophysics, 25:025015 (10pp), 2025 February
https://doi.org/10.1088/1674-4527/adab4b
CSTR: 32081.14.RAA.adab4b
© 2025. National Astronomical Observatories, CAS and IOP Publishing Ltd. All rights, including for text and data mining, AI training, and similar technologies, are reserved. Printed in China.

Detection of Emission Line Galaxies in the Slitless Spectra of HST and CSST

Kaiyuan Chen[1], Shuairu Zhu[2], Linhua Jiang[1,3], and Zhenya Zheng[2]
[1] Department of Astronomy, School of Physics, Peking University, Beijing 100871, China; jiangKIAA@pku.edu.cn
[2] Shanghai Astronomical Observatory, Chinese Academy of Sciences, Shanghai 200030, China
[3] Kavli Institute for Astronomy and Astrophysics, Peking University, Beijing 100871, China
Received 2024 November 17; revised 2025 January 2; accepted 2025 January 13; published 2025 February 10

Abstract

Slitless spectroscopy onboard space telescopes is a powerful tool to detect emission-line objects such as emission-line galaxies (ELGs) and quasars. In this work, we present a study of ELGs observed with slitless spectroscopy by the Hubble Space Telescope (HST) in a deep field of ∼44 arcmin^2. This is one of the deepest HST fields with a wealth of imaging and spectral data. In particular, previous VLT/MUSE observations have covered this field and identified a large number of ELGs. We reduce the HST spectra using the latest pipeline with a forward modeling algorithm and construct a sample of ELGs. By comparing with the MUSE spectra, we characterize our ELG detection in the HST spectra, including the impact of the line flux, line width, signal-to-noise ratio, etc. We find that the morphological broadening may affect the detection of ELGs, such that more compact sources are easier to be detected in slitless spectra. We discuss its implications to future slitless spectroscopic surveys that will be carried out by the China Space Station Telescope (CSST) and find that the CSST slitless spectroscopy has a capability comparable to that of HST in terms of the detection of emission lines.

Key words: techniques: spectroscopic – surveys – methods: data analysis – galaxies: general – galaxies: ISM

1. Introduction

Emission line galaxies (ELGs) are a valuable tool for studying star formation and exploring galaxy evolution (Kennicutt Robert 1992; Ballinger et al. 1996; Hopkins et al. 2003). For example, Balmer lines are common estimators of the star formation rate (SFR). H$\alpha\lambda$6563 is usually the most prominent line in local galaxies, and [O II] $\lambda\lambda$3726,3729 works as a good substitute when Hα is inaccessible in optical wavelengths for higher-redshift galaxies (Kewley et al. 2004). The combination of different lines reveals various galaxy properties, such as the Balmer Decrement for dust extinction corrections (Hao et al. 2011) and the "Baldwin, Phillips & Terlevich" diagram for AGN diagnosis (Baldwin et al. 1981). Large ELG catalogs from sky surveys make it possible to study cosmic evolution in a broader timescale. For example, Comparat et al. (2016) constructed emission line ([O II], Hβ, [O III] $\lambda\lambda$4959,5007) luminosity functions from ∼35,000 galaxies at $z \lesssim 1$ and found that the characteristic luminosity and peak number density increase with redshift. The rapid evolution of the Lyα luminosity function at cosmic dawn ($z \sim 6$) reflects the cosmic reionization history of the universe (Dijkstra et al. 2007; Santos et al. 2016).

To build a large and reliable sample of emission-line galaxies, efficient line identification methods are needed. One of the identification methods is slitless spectroscopy. It simultaneously captures the spectra of all sources in its field-of-view (FoV). There are also drawbacks. First, slitless spectroscopy works best in sparsely populated fields, but is less ideal for crowded fields. Overlaps of different 2D spectra result in contamination among sources (Kümmel et al. 2009). Second, the sky background is also dispersed by the grism or grating, bringing higher noise. Third, for sources with extended morphology, the emission line profiles can also become broadened (referred to as the morphological broadening hereafter), which results in a lower signal-to-noise ratio (SNR). Currently, these last two disadvantages can be mitigated in space telescope observations. In addition, excellent point-spread-function (PSF) in space minimizes the morphological broadening resulting from seeing. Consequently, slitless spectroscopy is currently employed and will continue to be used in many space telescope observations.

During the past few decades, Hubble Space Telescope (HST) carried out slitless spectroscopic surveys such as PEARS (Straughn et al. 2009; Pirzkal et al. 2013) and 3D-HST (Brammer et al. 2012; Momcheva et al. 2016). Since the launch of the James Webb Space Telescope (JWST), slitless spectroscopy has become more powerful. On JWST, both NIRISS and NIRCam implement wide-field slitless spectroscopy in the near-IR (Roberts-Borsani et al. 2022; Glazebrook et al. 2023). The resolution of the latter reaches approximately 1600 at 4 μm. They work in parallel with slit-spectroscopic observations or simultaneously with multi-band photometry (Sun et al. 2022; Yang et al. 2023; Backhaus et al. 2024; Helton et al. 2024). For example, in Backhaus et al. (2024), the slitless spectroscopy with NIRCam complements the high-z

galaxy sample observed with NIRSpec, including 19 galaxies with [O III]/Hβ measurements and 18 Hα emitters among 155 galaxies.

Currently, the China Space Station Telescope (CSST) is under development and is planned to be launched to a low Earth orbit (Zhan 2011, 2021). It will feature a 2 m diameter primary mirror with a $1.^{\circ}1 \times 1.^{\circ}2$ FoV, ~300 times larger than that of HST. The larger FoV enables its high efficiency in sky survey in the near-UV, u, g, r, i, z, and y bands. The slitless spectroscopy will include three bands (i.e., GU, GV, and GI). Their throughput curves are shown in Figure 7 in Zhan (2021). All CCDs will function simultaneously on the focal plane during observations. So, the aggregate exposure time depends on the number of CCDs assigned to the band. The slitless spectroscopy (taking up four CCDs for each band), in parallel with the photometry (with altogether 18 CCDs assigned), is planned to cover sky regions with an area of 17,500 deg^2 and a 400 deg^2 ultra-deep field, with spectral resolution $\gtrsim$200. For the previous 17,500 deg^2 sky region, the exposure time is planned to be 4×150 s per field, and 16×250 s per field for the latter. The GI grating can reach a depth of 24.3 mag in the AB system in the ultra-deep field. The magnitude here represents the aggregate flux of the grism spectrum. Three gratings carried onboard at that time can provide spectra for tens of millions of sources. The above characteristics help CSST perform effectively with respect to large-sky-area observations.

In this paper, we reprocess archival HST slitless spectroscopic data in a deep field. We discuss the effect of morphological broadening on emission line identifications and compare them with CSST forecast simulations. The structure of the paper is as follows. In Section 2, we introduce our data from HST and the emission line reference catalog from the MUSE-Wide (Urrutia et al. 2019) Sky Survey. We also give brief summaries of data reduction of HST G800L grism spectroscopy using the Grism Redshift and Line Analysis tool (GRIZLI[4]). In Section 3, we generate the simulated spectra for CSST observations and fit the emission lines in MUSE, ACS/G800L, and CSST/GI spectra. In Section 4, we compare the slitless spectroscopy using the ACS/G800L and the CSST/GI. We further discuss factors that influence their line detection capabilities, especially the morphological broadening effect. Section 5 summarizes our work.

2. Data and Data Reduction

Our data come from the GOODS-South region observed by both HST and the MUSE-Wide Survey. The observations in the GOODS sky regions were initiated in the 2000s, aiming for studies of galaxies, AGNs, and cosmology in multiple wavelengths (Treister et al. 2004; Bundy et al. 2005; Ravikumar et al. 2007). They include the North ($12^{\rm h}\ 36^{\rm m}\ 55^{\rm s}$, $+62^{\circ}\ 14'\ 15''$) and South ($03^{\rm h}\ 32^{\rm m}\ 30^{\rm s}$, $-27^{\circ}\ 48'\ 20''$) Sky regions, each $\sim 10' \times 16'$ in size. They are among the deepest regions observed, thus becoming pools of multi-wavelength data. Using ACS, both broad and narrow band photometry were performed in these fields. The GOODS HST Treasury Program imaged two GOODS fields in the B, V, i, and z bands, allocating 3, 2.5, 2.5, and 5 orbits for them, respectively. Using the narrow band image in F658N, Zhu et al. (2024) kept discovering new ELG candidates in recent years.

2.1. Data Archives

Large slitless spectroscopic surveys like PEARS and 3D-HST were carried out in these fields. Our raw spectroscopic data primarily come from these two programs. PEARS, conducted in Cycle 14, was allocated altogether 200 orbits for G800L spectroscopic survey and short F606W parallel photometry (Straughn et al. 2009). The grism survey consists of nine ACS Fields, including five fields in GOODS-South and four fields in GOODS-North. These programs employed a 2D line detection and extraction procedure that identified emission lines in the dispersed light beam images. There were finally 1162 Hα, [O III], and [O II] emission lines. 3D-HST aimed to find answers for a series of extra-galactic problems, including the mechanism that quenches star formation and the co-evolution of galaxies and their surroundings. It was allocated 248 orbits of HST time during Cycles 18 and 19 (Brammer et al. 2012). ACS/G800L and WFC3/G141 made the deepest exposures toward regions centered around ($03^{\rm h}\ 32^{\rm m}\ 30^{\rm s}$, $-27^{\circ}\ 48'\ 00''$). They took F814W and F140W direct images for two grism spectroscopy respectively, which was able to reach the depth comparable with deep ground-based photometry.

The information on exposures is given in Figure 1 and Table 1. The observation mode of spectroscopy on HST is composed of pre-image and grism exposure afterward. The former step serves at least three purposes. First, the pre-image provides high-accuracy photometry. Second, during data reduction, we use object positions on the pre-image and the dispersion function to trace 2D spectra, i.e., it is used for the wavelength calibration. Third, the integrated flux from photometry is used for the GRIZLI data reduction below.

In this study, we choose to reprocess the spectroscopic data instead of using the previously reduced data sets from the 3D-HST archive. The reasons are as follows. First, there are more observations in these fields after the 3D-HST program was completed. Pointings not far away can also overlap with the ~44 arcmin^2 region (like those in the PEARS survey). This increases the SNR of the spectra to identify fainter sources since GRIZLI is able to add up the 1D spectra from different position angles (PAs) with a unified wavelength calibration. Second, GRIZLI adopts a brand new data reduction method, i.e., the forward modeling (see Section 2 below for more details). This method improves the spectrum extraction quality,

[4] Available at https://github.com/gbrammer/grizli.

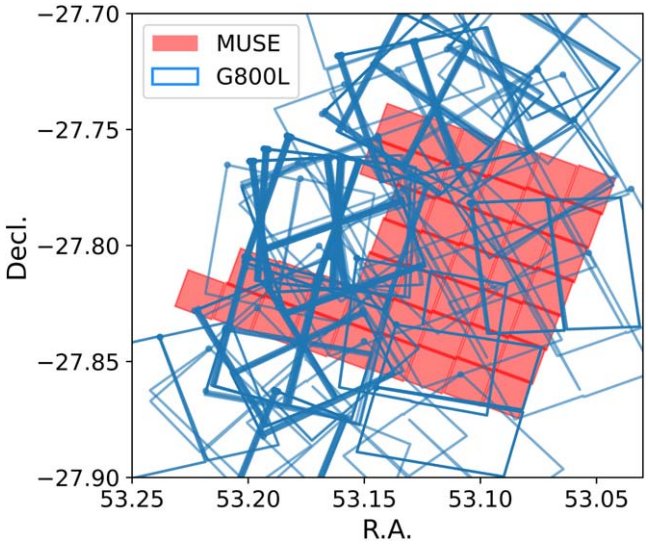

Figure 1. Observed sky region and depth using MUSE and G800L/ACS (a.k.a., Advanced Camera for Surveys, Anderson & Bedin 2010). The squares in red are sky regions observed with MUSE, each $1' \times 1'$ in size. The patches with blue edges stand for G800L exposures used in this work.

Table 1
ACS/WFC Exposures in Regions Studied

No.	Filter	P-ID	$N_{\rm exp}$	$T_{\rm exp}$ (s)
1	F606W	10189	6	3200
2	F606W	10530	27	9662
3	F606W	13779	4	2712
4	F775W	10189	13	7600
5	F814W	12177	18	8640
6	F850LP	13779	3	2034
7	F850LP	10189	20	21550
8	G800L	10189	14	32100
9	G800L	10530	99	218105
10	G800L	12177	19	59209
11	G800L	13779	6	23874

Note. Multi-band photometric and G800L exposures overlapped with the MUSE-Wide DR1. The names of the last three columns stand for the proposal ID, the number, and the aggregate time of exposures.

especially for overlapped spectra in densely populated fields. In Figure 2, we find that the emission line features in the 3D-HST products are weaker than those in the GRIZLI-reduced data. In consequence, the fitting procedure adopted in Section 3 fails for most 3D-HST sources due to low SNR. There are also fewer

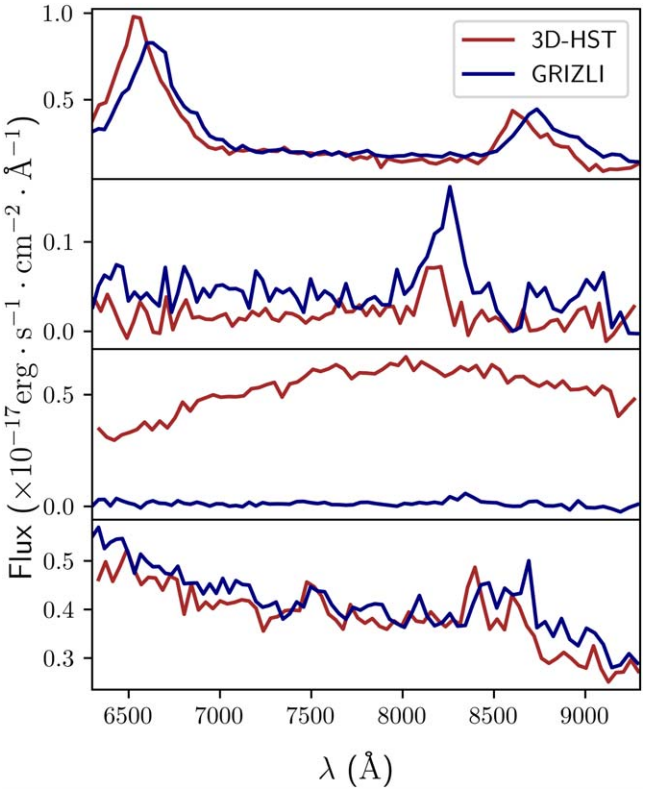

Figure 2. 3D-HST and GRIZLI reduced spectra of four sources. Through visual inspections, we can hardly identify emission line features in the lower three 3D-HST spectra. Whereas using GRIZLI, we identify four sources as ELGs. Among the four sources, the third one from the top shows the biggest difference between 2 spectra. We have inspected the 2D-spectrum from GRIZLI and the 3D image cut-out from MUSE, and have discovered a brighter source at the G800L wavelength range nearby. The lower flux of the GRIZLI spectrum, which is closer to the MUSE spectrum, further shows its advantage in contamination removal. In addition, this difference may also result from the different aperture radii adopted in the 1D-spectrum extractions.

2D spectra (only 570) for the ELGs identified by MUSE-Wide, from the 3D-HST products alone.

We choose the MUSE-Wide for a reference in this work, mostly due to its wavelength range (∼4800–9300 Å), largely in common with the G800L (∼5000–11000 Å) grism on HST and the GI grating (∼6300–10000 Å, see Section 1 for more details) on CSST. Using VLT, MUSE-Wide serves as the currently largest integrated field spectroscopic survey (Bacon et al. 2015). The blind survey program aims to minimize the source selection. It has a 1×1 arcmin^2 FoV in the wide survey mode. With a seeing of $\sim 0\farcs8$, it can reach a spatial sampling of 0.2×0.2 arcsec^2 with the help of the adaptive optics. The resolution varies from 1770 at 4800 Å to 3590 at 9300 Å. The one-hour exposure time for each unit makes it deep and accurate enough to reach the limiting magnitude of $I_{\rm AB} \simeq 22.28$. As a result, we choose the MUSE-Wide as an atlas for our analysis. The ∼44 arcmin^2 area ensures a sufficient

sample size. Currently, the public MUSE-Wide data is from 44 fields in the Chandra Deep Field South (Giacconi et al. 2001). There are altogether 1602 ELGs in the archive, almost all with photometric counterparts at multiple bands in the CANDELS catalog (Guo et al. 2013). In this work, we directly use the redshift information that the MUSE team provided on the emission line catalog.

2.2. G800L Data Reduction

Similar to Abramson et al. (2020), we use the `GRIZLI` pipeline (Wang et al. 2019) to extract spectra for all sources. Initially, we use the `MastQuery` Package to identify all G800L exposures targeting the studied region. Next, we identify all other G800L exposures and photometric exposures overlapped with the footprints of the previously mentioned exposures. This ensures that surrounding exposures and all sources at the edge of FoV are included. We download them from the MAST[5] website. All images are dark-subtracted and flat-fielded. Subsequently, we associate grism exposures with corresponding direct images, according to the visit, exposure order, and exposure footprints. Afterward, we run the `AstroDrizzle` Package (Gonzaga et al. 2012) to preprocess the images, including sky background subtraction, astrometric alignment, and image segmentation. In the meantime, we generate image mosaics, mask bad pixels, and remove cosmic rays (`Driz_CR`) by comparing multiple exposures in the same pointing. In addition, `GRIZLI` also runs the `L.A.Cosmic` Algorithm (Urrutia et al. 2019) to remove cosmic rays in single or double exposures, which is common for exposures near the Hubble Ultra-Deep Field (Beckwith et al. 2003). The algorithm aims to detect sharp flux changes between cosmic-ray-contaminated pixels and uncontaminated ones, and then mask the contaminated pixels. The removal process by `L.A.Cosmic` turns out to be less effective than that by `Driz_CR`. Therefore, we exclude the pointings with only one or two exposures to avoid fake emission line detections. We then derive a photometric catalog for reference in later steps and 2D cutouts of dispersed light beams for each position angle.

Next, we perform the 1D-spectrum extraction. `GRIZLI` calibrates the spectral wavelength on the 2D cutouts by applying the dispersion function to the center of the photometric source. This process may introduce systematic uncertainties in line identification, which we discuss in Section 4. Additionally, the pipeline will determine which order the dispersed beams are extracted according to their brightness. The algorithm considers factors such as the SNR, saturated or bad pixels, and spectral resolution. Typically, the first order is extracted because it retains most of the spectral energy.

Besides, there are situations where we need forward modeling, i.e., for sources with nearby contamination. We first sort all sources in densely populated regions in order of their magnitudes, according to the photometric catalog derived beforehand. We initially assume that each source has a flat continuum by averaging its integrated flux from the pre-image photometry. Starting from brighter ones, we build a polynomial continuum model for them and extract them with contamination removed (either the flat spectra of fainter neighbors or the polynomial models of brighter ones). We iterate the refinement repeatedly until we get clean 2D spectra.

Finally, spectra from different orders and position angles are combined, resampled, and reduced to 1D. Considering the sparsely populated sources and their brightness, we adopt the default optimal 1D-spectrum extraction method. The spectral resolution is about 100. Figure 3 portrays the 1D and 2D spectra of an object, together with its photometric information.

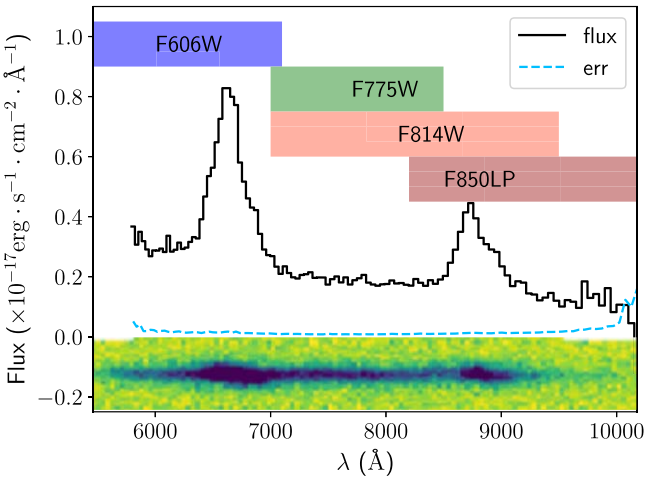

MUSE_ID	$z_{\rm MUSE}$	F606W	F775W	F814W	F850LP	$t_{\rm EXP}$(s)
102005037	0.34	22.2	22.5	22.3	22.0	6246

Figure 3. 1D and 2D spectra of a source in the ACS/G800L observation. Shadows with different colors stand for the wavelength coverage of multi-band photometry (blue for F606W, green for F775W, red for F814W, and brown for F850LP). The table below shows the ID in the MUSE Survey, MUSE-provided redshift, photometry in multiple bands (in the unit of magnitude), and the G800L exposure time (in the unit of second), respectively.

3. Results

In this section, we first describe the process of emission line identification in the MUSE-Wide spectra. We use the archived MUSE-Wide redshifts as preliminary redshifts to fit emission lines since its resolution and depth surpass those of the ACS/G800L and CSST/GI spectroscopy. With the fitted emission line and continuum model from the MUSE-Wide data, we generate simulated CSST grism exposures with the Python Package `Sls_1d_Spec`.[6] Afterwards, we repeat the previous

[5] https://mast.stsci.edu/

[6] https://csst-tb.bao.ac.cn/code/zhangxin/sls_1d_spec

line identification process on the ACS/G800L and simulated CSST spectra.

We first select emission line samples in the ACS/G800L archived data. We cross match all extracted G800L sources in the MUSE-Wide ELG catalog, which contains 1602 sources that have multi-band photometric counterparts provided by Guo et al. (2013). Each source typically exhibits different sizes in various bands. We require that selected G800L sources should be within the median Kron radii of their MUSE counterparts. Following the above rule, we select 885 spectra as the counterparts of the MUSE sources. Additionally, as mentioned in the cosmic-ray removal process in Section 2, G800L exposures in part of the $\sim$44 arcmin^2 region still have unremoved cosmic rays. Through visual inspection of their 2D spectra and their nearby sky regions, we keep 766 spectra of sources with cosmic rays properly removed. Using the archived redshifts from MUSE, we determine the wavelengths of the emission lines.

Next, we do the spectral line fitting using the Python Package "`Specutils`[7]" (Earl et al. 2023). Here we only consider strong emission lines between 6300 Å and 9300 Å (in the observed frame), i.e., [O II], Hβ, [O III], Hα (and [N II] $\lambda\lambda$6548,6583, if comparably strong). In this wavelength range, G800L can reach a high throughput of approximately 20% to 40%, so that the emission lines are more likely to be detected.

We do fitting for all 1602 MUSE spectra to build the intrinsic spectrum models for the CSST sources. We use a polynomial to fit the continuum, with possible emission line wavelength regions masked. For the continuum-subtracted spectrum of a source, we fit all emission lines at once using the L.M. Algorithm (Marquardt 1963). For strong emission lines (as mentioned above) with centers between 6300 and 9300 Å, we assign each line with a 1D Gaussian profile initially. With the redshift $z_{\rm M}$ measured by MUSE, we take $\lambda_{\rm rest} \times (1 + z_{\rm M})$ as the initial wavelength center. We take the flux peak as the initial guess for the amplitude. As to the line width, we adopt the initial σ parameter of 2 Å.

For the emission lines identified by MUSE, we require SNR $>$ 5. In this work, we refer to the SNR of the 2σ wavelength region on both sides by default. Because of the low spectral sampling rate of the ACS/G800L spectroscopy, the fitting procedure frequently fails if we adopt narrower line widths (e.g., the FWHM). For the [O III] doublet (similar to [N II]), we use the SNR of the stronger line or the de-blended stronger component. In addition, if Hα is identified, we fit them together with [N II] to include the [N II] flux in the simulated spectra below. We find that almost all selected emission lines match well with the catalog published on the MUSE website.

We use the modeled intrinsic spectra to generate the simulated CSST GI spectra with the Python Package `Sls_1d_Spec`.[8] The fitting model consists of a polynomial continuum and multiple emission lines ranging from 6300 to 9300 Å (see the dashed and colored lines in the upper panel of Figure 4). Instrumental broadening in MUSE spectra may slightly reshape the line profile. Since the spectral resolutions of both HST and CSST are significantly lower than that of MUSE, the few Å broadening in the MUSE spectra is negligible. We do not use the original MUSE spectra for two reasons. First, we assume a smooth profile for the spectra by nature. Noise in the observed MUSE spectra may impact the quality of the simulated CSST spectra. Second, the current version of `Sls_1d_Spec` requires a full spectral energy distribution in the UV, optical, and near-IR bands, so we extrapolate the continuum to the wavelength limit. We select the "GI" grating for its wavelength coverage and the first-order beam, which captures most of the dispersed spectral energy.

We inherit the default PSF, readout noise, dark field, pixel size, and sky background. For a fair comparison, we adopt the time and number of exposures from the G800L observations, which are roughly equal to the CSST deep field plan (i.e., 250 $\times$ 16 s). We do not generate CSST/GI spectra for the MUSE ELGs without G800L detections. In real CSST/GI observations, there would also be undetected sources, e.g., due to non-detection in photometry, or the position at the edge of CCDs. For simplicity, we adopt a Sérsic index of $n = 1$, a position angle of PA $= 45°$, and an axis ratio of $q = 1$ for galaxies in our simulations. We take 0.4 times the median Kron radii, i.e., the first moment radius of the ACS photometry in optical bands, as the intrinsic effective radius of the source. `Sls_1d_Spec` adds in the PSF of GI spectroscopy (FWHM $\simeq 0\farcs39$), which surpasses that of ACS photometry.

We disperse the spectral energy according to the above parameters spectrally and spatially. After adding up the simulated sky background, the Poisson noise, the instrumental noise, etc., we derive the simulated 2D spectra. Given the beam order, at each wavelength, `Sls_1d_Spec` takes increasing aperture radius spatially, until the sum reaches 90% of the real aggregate flux. We sum up the flux within the aperture radius and reduce the spectra to 1D. The 1D spectra of the four sources are shown in the lower panels of subfigures in Figure 4.

Similar to the fitting procedure of the MUSE spectra, we do line fitting for the G800L and simulated CSST data. We take the initial guess of amplitude and wavelength center in the same way as previously. Considering their resolutions are lower than that of MUSE, we take 80 Å and 40 Å as the initial σ for G800L and CSST/GI, respectively. Primarily due to the lower resolution, some distinct emission lines become broadened and difficult to distinguish from the continua. In consequence, we require the σ smaller than 150 Å for the ACS/

[7] https://specutils.readthedocs.io/en/stable/index.html

[8] https://csst-tb.bao.ac.cn/code/zhangxin/sls_1d_spec

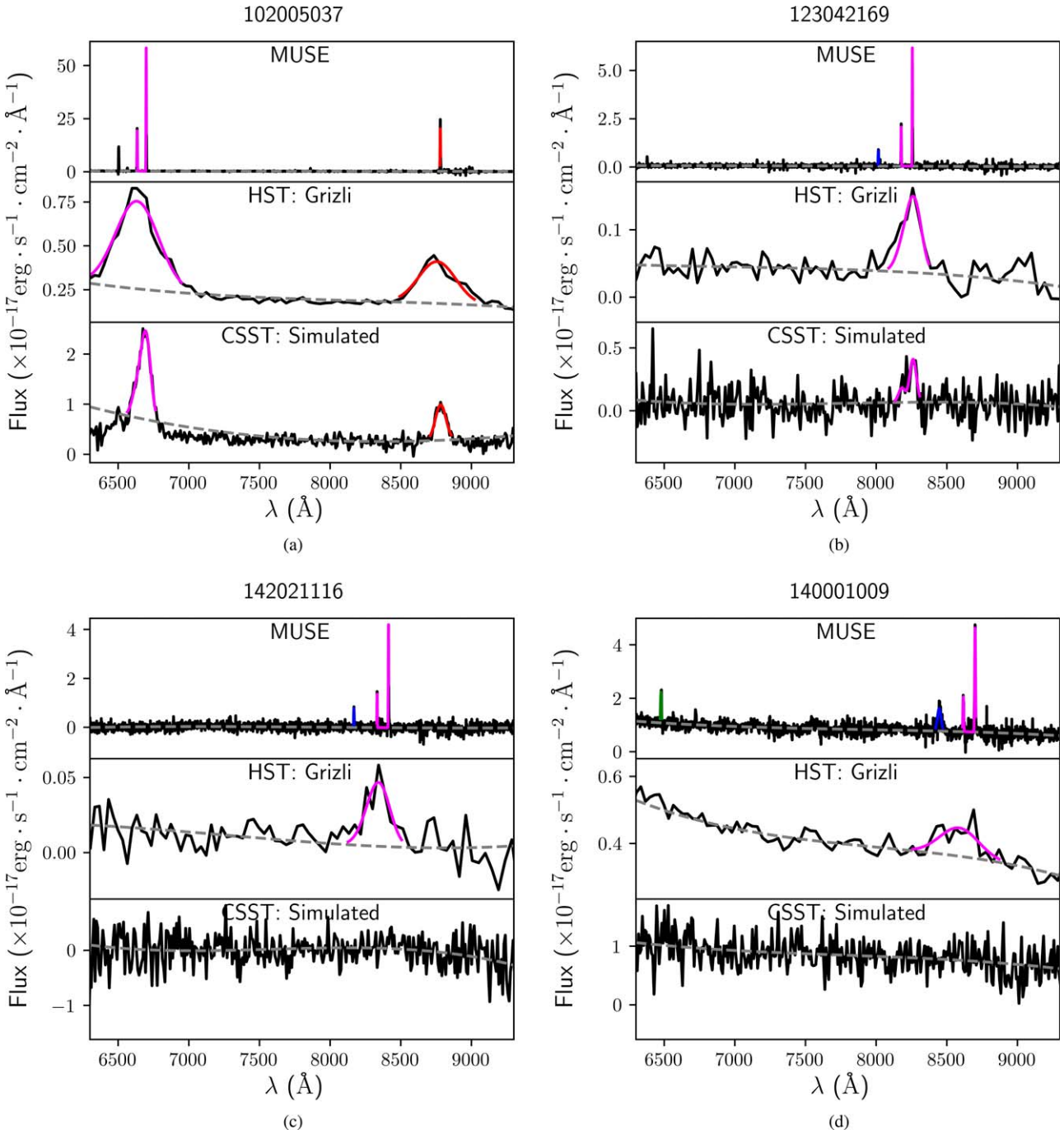

Figure 4. MUSE, ACS/G800L, and simulated CSST spectra of four sources (titles of the subfigures show their IDs in the MUSE survey). They also correspond to the four sources in Figure 2 from top to bottom, respectively. Colored lines are the Gaussian model fitting of emission lines (red for Hα, blue for Hβ, and magenta for [O III]). The [O III] line flux in the first three subfigures decreases in order. Note that in slitless spectroscopy, due to the spectral resolution and the morphological broadening, the Hβ line is usually blended with the nearby [O III].

G800L, and 75 Å for the CSST/GI. We require SNR $>$ 5 for both slitless spectroscopy. Hβ and [O III] are usually blended in the G800L spectra because of the lower resolution. We are only able to de-composite them with the spectral line fitting in some of the spectra. Thus, Hβ or [O III] identified in the G800L spectra may consist of the flux of both lines. Hα is closer to the [N II] doublets on both sides and usually much stronger. As a result, we directly take Hα together with two [N II] doublets as

a single line in both G800L and CSST/GI spectra. All lines identified by MUSE and G800L or GI are listed in Table 2.

4. Discussion

In this section, we first compare the line detection of the ACS/G800L spectra and that of the simulated CSST/GI spectra. Afterward, we discuss the morphological broadening effect on the spectral line profile (the σ parameter). While previous simulations have explored this broadening effect (Wen et al. 2024), we find that various factors during the data reduction process lower the obtained SNR, such as cosmic rays and overlapping spectra. Hence, it is helpful to illustrate this effect using the HST data.

4.1. CSST Detection Efficiency

In this subsection, we compare the detection efficiency between the observed HST spectroscopy and the simulated CSST spectroscopy, given the same exposure time. HST observations share a lot of similarities with CSST. Both telescopes work at low Earth orbit and with a similar size in diameter ($\gtrsim$2 m), which means they have a similar chance affected by cosmic rays. As shown in Table 2, G800L has a total of 33 lines identified with SNR $>$ 5, whereas the simulated CSST observations only have 22.

It seems that HST G800L has better performance. However, there are various factors that may influence the efficiency of slitless spectroscopy. First, as mentioned in the above paragraph, masked cosmic rays and bad pixels shorten the actual exposure time. Considering this, the SNR of emission lines from CSST/GI will decrease.

The second factor is the spectral resolution and the pixel scale. Due to the lower resolution of G800L, some blended lines are mistaken as a single line, which introduces additional systematic uncertainties. For example, for the source in Figure 4(a), the identified [O III] line consists of both Hβ and [O III]. Therefore, the SNR is overestimated. For the CSST/GI spectra, the current `Sls_1d_Spec` adopts a resolution at $\gtrsim$200, but the CCD sampling is about 10 Å per pixel. Hence, the SNR of CSST detection can be enhanced if we can adjust the CCD sampling size (e.g., bin pixels).

Third, the source radius taken in 2D-spectrum generation affects the line profile. In this work, we directly adopt the first moment radius of the source from multi-band photometry as the effective radius (see Section 3) and the `Sls_1d_Spec` distributes the spectral energy according to the Sérsic profile. In reality, on the 2D spectra of more extended sources (e.g., mergers, a rare case), in the spatial direction, the gas clouds that generate emission lines may be located more distant from the central region (Arroyo-Polonio et al. 2023). Thus, part of the emission line flux would not be taken into the 1D-spectrum reduction. More important, spectrally, the gas cloud distribution results in a broadened line profile (see Section 4.2 below for more details) and correspondingly more noise included. Many high-flux emission lines from low-z galaxies (the 2D profile of which is usually more extended) thus vanish in the continua. Down to ELGs in Table 2, we find that most of the sources with $r_{\rm Kron} > 1''$ exhibit compact emission line regions in MUSE observations (e.g., see Figure 7(b), $\gtrsim$75% of the line flux concentrates within the central region of $0''.5$ in radius). Considering the smaller PSF in space, the observed emission line regions will be more compact. Hence, the simulation above overestimates the morphological broadening effect (see Section 4.2 below) in the GI spectra. In the table, ACS/G800L and CSST/GI spectroscopy have similar performance in detecting ELGs with $r_{\rm Kron} \lesssim 1''$. The latter even makes two more detections. As a result, we attribute the difference in performance of the instruments mostly to this factor.

Finally, in this work, we know the source redshifts beforehand using the MUSE-Wide DR1. In real observations, due to lower resolution and shorter wavelength coverage, fewer emission lines can be confirmed, which gives rise to uncertainties in the redshift estimation. In consequence, even if we have line signals detected, it is harder for us to identify their nature. This also favors CSST/GI, which is endowed with a higher resolution ($\gtrsim$200). For instance, we can distinguish between the Hβ and the [O III], if both have a strong enough SNR and the source is compact (see the upper two panels in Figure 5(a)).

4.2. Morphological Broadening

We first describe the morphological broadening effect. When a resolved 2D object is dispersed, photons received in one pixel may come from different parts of the source (which are mapped to different pixels in photometry). Photons away from the source center will "blueshift" or "redshift" to other wavelengths during the calibration. As a result, emission lines in slitless spectroscopy are broadened depending on the source's 2D size. Here, we use the pixel size to represent the PSF of the grating observation, i.e., $0''.074$ for the current CSST/GI design. In Figure 5, if the source is point-like (with an intrinsic angular size $r_e \lesssim 0''.074$), the instrumental broadening dominates and the line profile hardly changes. If r_e increases, the SNR quickly drops along with the broadened line profile. When r_e increases to $\sim 1''$, the morphological broadening becomes significant. Thus, the line fitting is less accurate. It gives rise to the non-monotonical growth of the curve in the right panel. From the left panel, when the object size is equivalent to the CSST PSF size, we see two components of the [O III] doublet. When it reaches $0''.2$, [O III] appears as a single line. As it goes up to $0''.5$, [O III] is even blended with the Hβ. This morphological effect also adds to the uncertainties in the wavelength calibration, when the flux center deviates from the geometric center of the source.

Table 2
Line Fitting Results

MUSE_ID	Line	$r_{\rm Kron}$ ($''$)	MUSE Measurements			ACS/G800L Measurements					CSST GI		
			EW (Å)	z	SNR	z	FWHM (Å)	SNR	$T_{\rm exp}$ (s)	$N_{\rm exp}$	z	FWHM (Å)	SNR
102005037	Hα	0.83	421	0.338	153	0.33	322	45	6246	8	0.34	88	26
102005037	[O III]	0.83	506	0.338	1456	0.33	324	74	6246	8	0.34	75	45
102021103	Hα	0.81	44	0.247	162	⋯	⋯	⋯	4617	6	0.25	69	7
102027126	[O II]	0.60	159	1.128	62	1.12	140	5	3123	4	1.13	94	7
102032148	[O III]	0.69	391	0.666	44	0.65	117	5	3123	4	⋯	⋯	⋯
102047173	[O II]	0.73	154	0.963	46	⋯	⋯	⋯	3123	4	0.96	108	5
102050177	[O II]	0.64	143	1.004	65	1.02	353	5	3123	4	⋯	⋯	⋯
105002016	Hα	1.13	96	0.343	365	0.35	353	27	16052	16	0.34	96	44
106001006	Hα	0.76	97	0.288	65	⋯	⋯	⋯	5423	6	0.29	68	7
106002013	Hα	0.97	50	0.288	69	⋯	⋯	⋯	5423	6	0.29	94	6
106005027	Hα	0.65	104	0.388	92	0.38	228	6	5423	6	⋯	⋯	⋯
106005027	[O III]	0.65	50	0.388	33	0.39	175	17	5423	6	0.39	56	5
106024064	[O III]	0.68	63	0.671	84	0.66	353	8	5423	6	0.67	66	7
107025121	Hβ	0.68	201	0.730	10	0.73	353	6	3123	4	⋯	⋯	⋯
107025121	[O III]	0.68	1016	0.730	35	0.73	176	8	3123	4	⋯	⋯	⋯
107029135	[O II]	0.89	71	0.736	104	⋯	⋯	⋯	5423	6	0.73	90	7
111008017	[O III]	0.75	117	0.668	43	0.67	353	12	9823	10	0.67	74	8
112009047	[O III]	1.04	63	0.578	170	⋯	⋯	⋯	6246	8	0.58	83	8
113001007	Hα	1.31	145	0.232	326	⋯	⋯	⋯	6246	8	0.23	117	11
113004019	Hα	1.00	69	0.339	57	⋯	⋯	⋯	9369	12	0.34	69	8
113006027	Hα	0.85	19	0.129	71	0.14	209	7	6246	8	⋯	⋯	⋯
113010038	Hβ	0.98	2	0.576	8	0.56	353	6	9369	12	⋯	⋯	⋯
117007029	Hβ	0.68	117	0.523	43	0.52	144	5	2400	4	⋯	⋯	⋯
117007029	[O III]	0.68	531	0.523	258	0.53	155	18	2400	4	0.52	57	8
117023068	[O II]	0.66	147	0.980	160	⋯	⋯	⋯	2400	4	0.98	118	6
117046098	[O II]	0.64	159	1.389	45	⋯	⋯	⋯	2400	4	1.38	87	6
118003015	Hα	0.72	28	0.214	24	0.23	340	6	2400	4	⋯	⋯	⋯
122003050	Hα	1.56	45	0.214	213	⋯	⋯	⋯	3123	4	0.22	133	11
123012110	[O III]	0.67	50	0.545	200	0.57	353	6	2400	4	0.55	75	6
123042169	[O III]	0.61	448	0.649	185	0.65	121	11	2400	4	0.65	56	6
124002008	Hα	0.85	40	0.242	204	0.24	353	8	3123	4	0.24	117	10
129016132	[O III]	3.37	200	0.772	15	0.78	353	6	6246	8	⋯	⋯	⋯
131005052	Hα	3.07	93	0.331	21	0.33	210	7	9823	10	⋯	⋯	⋯
131009089	Hβ	4.00	9	0.363	77	0.38	353	6	7523	8	⋯	⋯	⋯
131009089	Hα	4.00	77	0.363	127	0.37	353	23	7523	8	⋯	⋯	⋯
132021040	Hβ	5.36	21	0.523	17	0.52	269	10	3123	4	⋯	⋯	⋯
134038060	[O III]	3.55	1430	0.544	24	0.54	119	7	9369	12	⋯	⋯	⋯
135035225	[O II]	3.00	2582	0.998	5	1.00	172	10	7740	10	⋯	⋯	⋯
137031068	[O III]	3.50	435	0.544	159	0.56	223	17	3123	4	⋯	⋯	⋯
139009211	Hα	4.02	94	0.366	278	0.36	100	5	6246	8	⋯	⋯	⋯
140001009	[O III]	4.58	36	0.737	51	0.72	311	9	3123	4	⋯	⋯	⋯
142021116	[O III]	4.76	-868	0.680	43	0.67	200	7	3123	4	⋯	⋯	⋯
143028101	[O III]	3.45	1235	0.705	34	0.70	119	11	9823	10	⋯	⋯	⋯
143052137	[O II]	4.42	244	1.234	25	1.23	135	6	9823	10	⋯	⋯	⋯

Note. Information of MUSE emission lines with HST or CSST detection (SNR > 5). Column "$r_{\rm Kron}$" is the median value of the Kron radius measured in multiple bands. "EW" is the equivalent width of the emission line. "$T_{\rm exp}$" and "$N_{\rm exp}$" are the aggregate time and numbers of ACS/G800L exposures, respectively, and are also adopted for the CSST simulation. The EW of one emission line is negative because the line is located near the end of the MUSE wavelength range ($\gtrsim$9000 Å), and the continuum is estimated below zero. For all Hα lines, the flux used for computing EW includes that of the [N II], similar for the FWHM and SNR in both G800L and GI spectra.

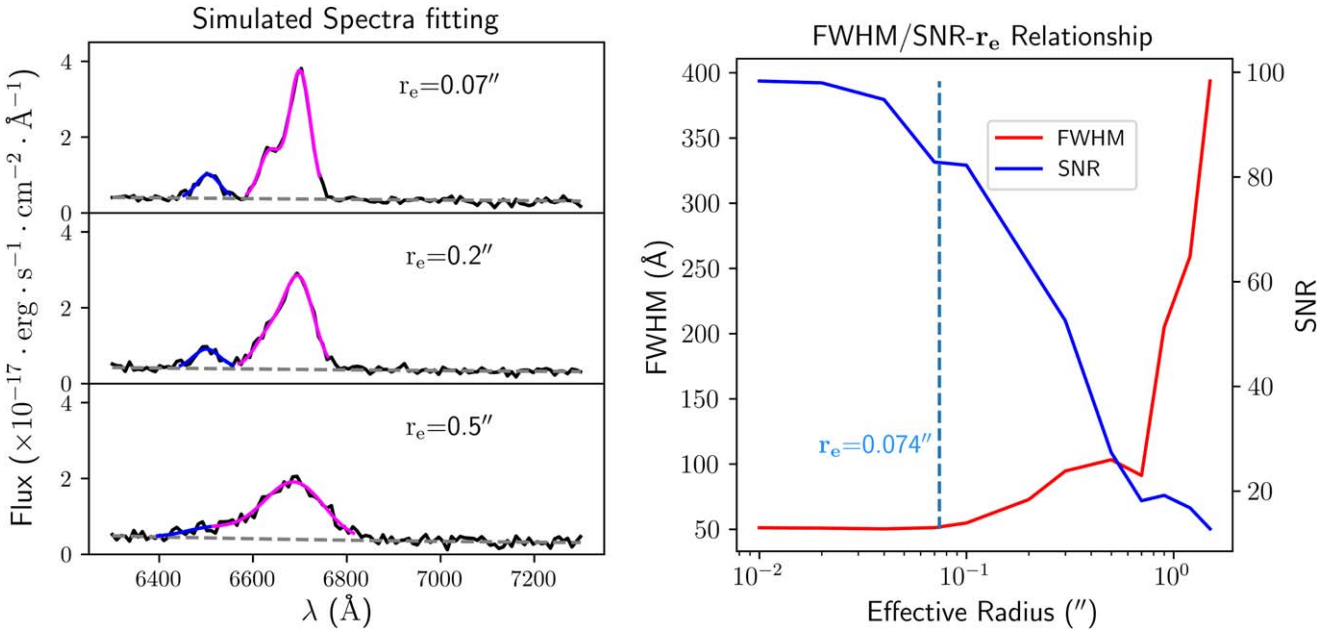

Figure 5. Line fitting results with different effective radii, using CSST simulation data. The spectrum model and all the other parameters needed are adopted from the source in Figure 4(a). The left figure shows three typical occasions on which the angular size of the source $\lesssim$, $\gtrsim$, and $\gg$ the pixel scale. The right figure illustrates the change of [O III] FWHM and SNR with different r_e adopted. The vertical dashed line labels out the pixel scale currently designed for CSST. Note that the effective radii adopted here are the intrinsic angular sizes of the simulated source. The PSF of the instrument is calculated otherwise.

Regarding real observations, we find that the ACS/G800L favors more compact sources given the same redshift range. We still use the MUSE data for comparison. The morphological broadening has minimal impact on MUSE observations since the whole galaxy was divided into hundreds of subsets to generate data cubes. Each data cube had its own wavelength calibration. This implies that, given the same exposure depth, slitless spectroscopy may be more likely to miss lower-z sources, which are typically more extended, compared to unbiased integral-field spectroscopy. Powered by star-forming activities, the H II region usually exists broadly across ELGs (Sánchez et al. 2012; López-Hernández et al. 2013), so we choose ELGs in the redshift range $0 \sim 0.42$ and with Hα detection. Their Kron radius distribution is shown in the histogram in Figure 6. The mean Kron radii are $\sim 2\farcs2$for MUSE and $\sim 1\farcs8$ for ACS/G800L.

Additionally, we find that for extended sources with G800L detections, the [O III] line region is usually more compact than the continuum emission region (see Figure 7). Previous integral-field observations also discovered a hot, ionized, gaseous component in the central region of some galaxies (Kehrig et al. 2016; Ilha et al. 2024), which is possibly produced by active galactic nuclei winds. As a result, it alleviates the morphological broadening effect on the [O III] line detection.

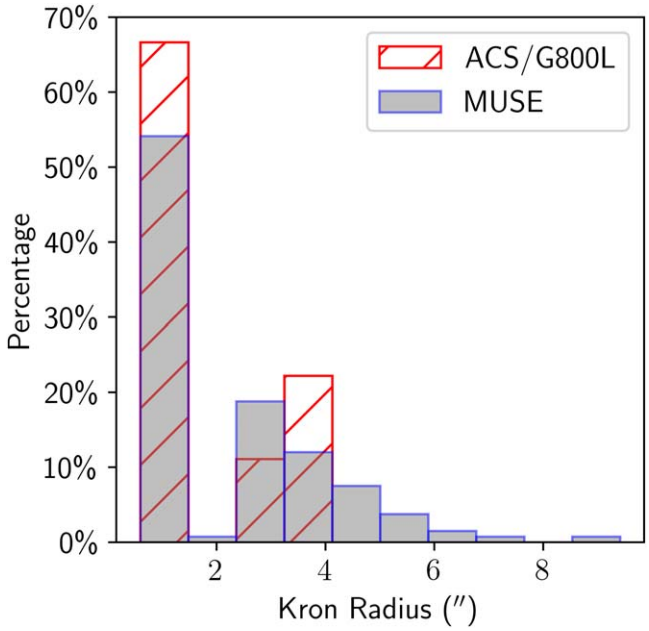

Figure 6. The Kron radius distribution of ELGs with Hα identified and redshift lower than 0.42, using MUSE-Wide DR1 (the gray patch) and ACS/G800L archive data (the red shadowed patch).

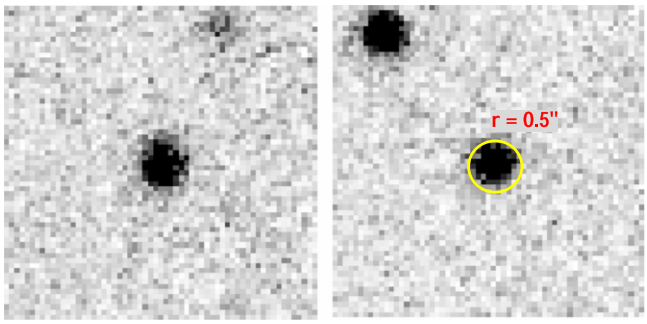

Figure 7. The 2D cut-out of sources in Figures 4(c) and (d) from the MUSE-Wide data cube, at their [O III] wavecenter. Both images are $6'' \times 6''$. Both sources have a Kron radius (i.e., continuum energy distribution) $\lesssim 5''$ but the [O III] emission concentrates in $r \lesssim 0.''5$ sky region. The seeing during the observation rests at $\sim 1''$ (Urrutia et al. 2019).

5. Summary

In this work, we reduced the ACS/G800L slitless spectroscopic data using the latest pipeline `Grizli`. The pipeline applied forward modeling to extract overlapped spectra. Our data are from HST observations that cover the $\sim$44 arcmin^2 MUSE-Wide region in the GOODS-South Field. After continuum subtraction, we fitted the lines ([O II], Hβ, [O III], Hα, and [N II]) for the MUSE spectra using Gaussian models. Next, we used the fitted MUSE spectrum models to generate simulated CSST/GI spectra. After that, we fitted the G800L spectra and the simulated CSST spectra in the same way as above.

We identified 33 emission lines with SNR > 5 in the G800L observations and 22 in the CSST/GI simulated spectra. We compared the two sets of spectra. In terms of emission line detection, CSST had a capability comparable to HST. In addition, the emission line region morphology from MUSE-Wide suggested that CSST/GI might achieve a better performance in real observations. Higher spectral resolution and larger FoV further enhance the efficiency of CSST grism spectroscopy in sky surveys.

The ELG detection capability of slitless spectroscopy aboard space telescopes may be compromised for various reasons, including cosmic rays, spectral resolution, and morphological broadening. We then briefly analyzed how source morphology influences line detection and its profile using the G800L and simulated GI spectroscopy. Sources with more compact emission line regions were favored. This work provided a forecast for slitless spectroscopy and ELG identification in future CSST observations.

Acknowledgments

We acknowledge support from the National Key R&D Program of China (2022YFF0503401), the China Manned Space Project with No. CMS-CSST-2021-A05, and the National Natural Science Foundation of China (12225301).

ORCID iDs

Kaiyuan Chen https://orcid.org/0000-0003-3536-5504

References

Abramson, L. E., Brammer, G. B., Schmidt, K. B., et al. 2020, MNRAS, 493, 952
Anderson, J., & Bedin, L. R. 2010, PASP, 122, 1035
Arroyo-Polonio, A., Iglesias-Páramo, J., Kehrig, C., et al. 2023, A&A, 677, A114
Backhaus, B. E., Trump, J. R., Pirzkal, N., et al. 2024, ApJ, 962, 195
Bacon, R., Brinchmann, J., Richard, J., et al. 2015, A&A, 575, A75
Baldwin, J. A., Phillips, M. M., & Terlevich, R. 1981, PASP, 93, 5
Ballinger, W. E., Peacock, J. A., & Heavens, A. F. 1996, MNRAS, 282, 877
Beckwith, S. V. W., Caldwell, J., Clampin, M., et al. 2003, AAS Meeting, 202, 17.05
Brammer, G. B., van Dokkum, P. G., Franx, M., et al. 2012, ApJS, 200, 13
Bundy, K., Ellis, R. S., & Conselice, C. J. 2005, ApJ, 625, 621
Comparat, J., Zhu, G., Gonzalez-Perez, V., et al. 2016, MNRAS, 461, 1076
Dijkstra, M., Wyithe, J. S. B., & Haiman, Z. 2007, MNRAS, 379, 253
Earl, N., Tollerud, E., O'Steen, R., et al. 2024, astropy/specutils: v1.19.0
Giacconi, R., Rosati, P., Tozzi, P., et al. 2001, ApJ, 551, 624
Glazebrook, K., Nanayakkara, T., Jacobs, C., et al. 2023, ApJL, 947, L25
Gonzaga, S., Hack, W., Fruchter, A., & Mack, J. 2012, The DrizzlePac Handbook (Baltimore, MD: STScI)
Guo, Y., Ferguson, H. C., Giavalisco, M., et al. 2013, ApJS, 207, 24
Hao, C.-N., Kennicutt, R. C., Johnson, B. D., et al. 2011, ApJ, 741, 124
Helton, J. M., Sun, F., Woodrum, C., et al. 2024, ApJ, 962, 124
Hopkins, A. M., Miller, C. J., Nichol, R. C., et al. 2003, ApJ, 599, 971
Ilha, G. S., Krabbe, A. C., Riffel, R. A., et al. 2024, MNRAS, 532, 2988
Kehrig, C., Vílchez, J. M., Pérez-Montero, E., et al. 2016, MNRAS, 459, 2992
Kennicutt Robert, C. J. 1992, ApJ, 388, 310
Kewley, L. J., Geller, M. J., & Jansen, R. A. 2004, AJ, 127, 2002
Kümmel, M., Walsh, J. R., Pirzkal, N., Kuntschner, H., & Pasquali, A. 2009, PASP, 121, 59
López-Hernández, J., Terlevich, E., Terlevich, R., et al. 2013, MNRAS, 430, 472
Marquardt, D. W. 1963, J. Soc. Ind. Appl. Math., 11, 431
Momcheva, I. G., Brammer, G. B., van Dokkum, P. G., et al. 2016, ApJS, 225, 27
Pirzkal, N., Rothberg, B., Ly, C., et al. 2013, ApJ, 772, 48
Ravikumar, C. D., Puech, M., Flores, H., et al. 2007, A&A, 465, 1099
Roberts-Borsani, G., Morishita, T., Treu, T., et al. 2022, ApJL, 938, L13
Sánchez, S. F., Rosales-Ortega, F. F., Marino, R. A., et al. 2012, A&A, 546, A2
Santos, S., Sobral, D., & Matthee, J. 2016, MNRAS, 463, 1678
Straughn, A. N., Pirzkal, N., Meurer, G. R., et al. 2009, AJ, 138, 1022
Sun, F., Egami, E., Pirzkal, N., et al. 2022, ApJL, 936, L8
Treister, E., Urry, C. M., Chatzichristou, E., et al. 2004, ApJ, 616, 123
Urrutia, T., Wisotzki, L., Kerutt, J., et al. 2019, A&A, 624, A141
van Dokkum, P. G., Bloom, J., & Tewes, M. 2012, L.A.Cosmic: Laplacian Cosmic Ray Identification, Astrophysics Source Code Library, ascl:1207.005
Wang, X., Jones, T. A., Treu, T., et al. 2019, ApJ, 882, 94
Wen, R., Zheng, X. Z., Han, Y., et al. 2024, MNRAS, 528, 2770
Yang, J., Wang, F., Fan, X., et al. 2023, ApJL, 951, L5
Zhan, H. 2011, SSPMA, 41, 1441
Zhan, H. 2021, ChSBu, 66, 1290
Zhu, S., Zheng, Z.-Y., Rhoads, J., et al. 2024, ApJS, 271, 5